Scientific Research Publishing

Journal of Power and Energy Engineering, 2022, 10, 45-67
https://www.scirp.org/journal/jpee
ISSN Online: 2327-5901
ISSN Print: 2327-588X

Investigating the Effects of Interface Topology on Flow Development in Rod Bundle Supported by Spacer Grid with Split Mixing Vane Using STAR-CCM+

Vincent Yao Agbodemegbe[1], Edward Shitsi[1,2*], Felix Ameyaw[1,3], Henry Cecil Odoi[1,2], Isaac Kwasi Baidoo[1,2]

[1]School of Nuclear and Allied Sciences, University of Ghana, Accra, Ghana
[2]National Nuclear Research Institute, Ghana Atomic Energy Commission, Accra, Ghana
[3]Nuclear Power Institute, Ghana Atomic Energy Commission, Accra, Ghana
Email: vincevalt@gmail.com, *edwardshitsi@hoo.com, fafeknoc@yahoo.co.uk, hencilod@gmail.com, baidooisaac51@yahoo.co.uk

How to cite this paper: Agbodemegbe, V.Y., Shitsi, E., Ameyaw, F., Odoi, H.C. and Baidoo, I.K. (2022) Investigating the Effects of Interface Topology on Flow Development in Rod Bundle Supported by Spacer Grid with Split Mixing Vane Using STAR-CCM+. *Journal of Power and Energy Engineering*, **10**, 45-67.
https://doi.org/10.4236/jpee.2022.1011004

Received: October 20, 2022
Accepted: November 27, 2022
Published: November 30, 2022

Abstract

Flow development downstream of a spacer grid is dependent on the upstream conditions and the imposed interface topology, especially at inlet and outlet boundaries. In STAR-CCM+, all interfaces fall into two groups, direct and indirect. A direct interface directly joins together two boundaries composing the interface either permanently or temporarily, for the case of rigid body motion. An explicit connection is created between cells on each side of the interface, so that mass and energy or either of them will occur across the interface. Three options of interface topology namely, in-place, periodic and repeating are available to be imposed at the inlet-outlet boundaries for a flow problem. In the present work, computational fluid dynamic simulation using STAR-CCM+ was performed for the flow of water at a bundle's Reynolds number of Re1 = 3.4×10^4 through a 5×5 rod bundle geometry supported by spacer grid with and without split mixing vanes for which the rod-to-rod pitch to diameter ratio was 1.33 and the rod to wall pitch to diameter ratio was 0.74. The two-layer k-epsilon turbulence model with an all y+ automatic wall treatment function in STAR-CCM+ was adopted for an isothermal single phase (water) flow through the geometry with and without imposed cyclic periodic interface boundary condition of fully developed flow type at inlet and outlet boundaries. The objectives were to primarily investigate the extent of predictability of the experimental data by the Computational Fluid Dynamic (CFD) simulation as a measure of reliability on the CFD code employed, and

also study the effects of the imposed interface topology on flow redistribution in the presence and absence of split mixing vane. Validation of simulation results with experimental data showed a good correlation of mean flow parameters with experimental data. Generally, the agreement of simulation results with data obtained from the experimental investigation confirmed the suitability of the CFD code, STAR-CCM+ to analyze the physical problem considered. Trends of flow redistribution downstream of the spacer grid indicate that, the split mixing vanes acted to quickly bring the flow to an equitable redistribution downstream of the spacer grid irrespective of the imposed inlet-outlet interface topology. For the case of the spacer grid without mixing vanes, some extents of deviation were realized between the model with no imposed interface topology and that with imposed periodic interface topology. The variation in trends shows that, a much longer inlet segment of the domain is required to completely nullify the effect of the inlet-outlet interface topology on flow distribution in the absence of mixing vanes which may lead to a relatively higher demand for computational resources than required in the presence of mixing vanes.

Keywords

CFD, Spacer Grid, Split Vane, Interface Topology, Turbulence, STAR-CCM+

1. Introduction

The use of Computational Fluid Dynamics (CFD) for nuclear applications is promoted internationally by the Organization for Economic Cooperation and Development (OECD) through its Nuclear Energy Agency [1]. The CFD approach for analysis and design is enhanced by the application of best practice guidelines for simulations and which does not invalidate a final but essential step of verifying the CFD simulation results through a few experiments than before. Currently, the application of CFD codes in predicting single-phase flows in rod bundles still faces challenges due to the difficulties in accurately predicting turbulent structures such as secondary flows, vortex shedding and flow pulsations that contribute to inter-sub-channel mixing [1] [2] [3]. Current computational methods can not be fully trusted in complex applications and still require significant development of new models as well as thorough validation of the existing models [4]. Among the contributing factors to these failures is the inability to develop an optimal mesh that appropriately captures the turbulent structures at the relevant points in the flow domain. To obtain any fine details during CFD simulations, the high-density mesh of appreciable quality is required over the extent of the computational domain and especially at the location of interest. This requirement in turn poses high computational resource demand which in many cases is limited.

To overcome this shortcoming, shorter segments of the full domain are modeled with imposed periodic interface topology of fully developed type at inlet and

outlet boundaries. The boundaries for a periodic interface are separated in space but can be mapped from one to the other through some constant rotation or translation, and it represents a cyclic repeat of information across the boundaries, so that fluxes that cross one boundary are transformed and applied to the other boundary [5]. The approach effectively approximates a repeating geometry and makes it possible to model an infinitely long pipe by just using a short segment of the pipe [5], and therefore, reduces the computational resource demand for CFD simulations.

In the present study, two interface boundary conditions were imposed to study their effect on the development of flow downstream of a spacer grid with and without mixing vanes. A uniform mass flow inlet condition without the imposition of a cyclic periodic boundary condition at the inlet-outlet boundaries was simulated and the results were compared to data obtained when a Cyclic Periodic interface Boundary Condition (CPBC) or topology was applied at both inlet and outlet boundaries of the domain with a fully developed interface type. **Figures 1-3** show a generic design of the split-type spacer grid, the split mixing vane arrangement and the detailed dimension of the mixing vanes respectively that were used to support the rod bundles for the present work.

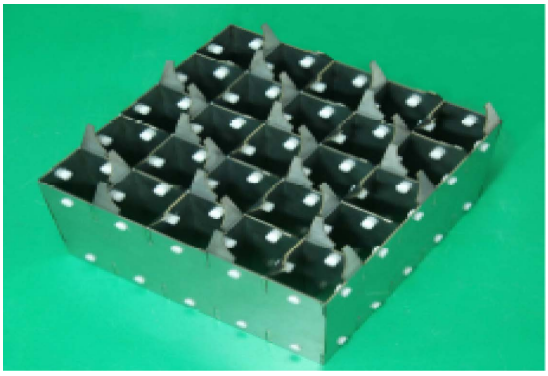

Figure 1. Split-type spacer grid [6].

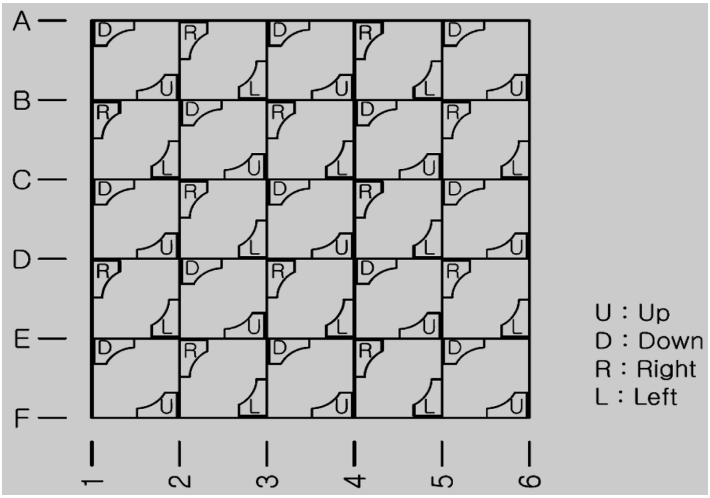

Figure 2. Split-type spacer grid [6].

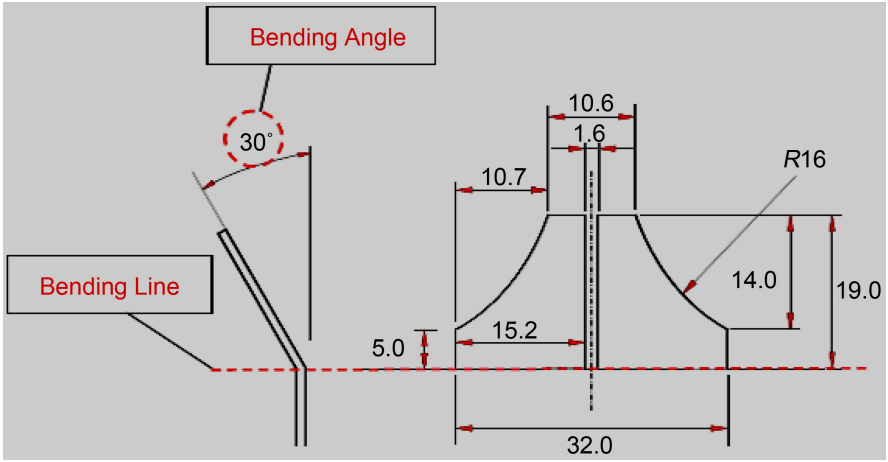

Figure 3. Detailed dimensions of split mixing vane [6].

Spacer grids with various types of attached vanes to promote turbulence mixing are designed as a support for the fuel rods. When used to provide mechanical support, spacer grids reduce flow-induced vibration [7], and also absorb any vibration impact during the process of loading, shipping and handling of the fuel assemblies. The split-type mixing vanes serve as flow deflectors attached to the spacer grid to improve lateral convection, and hence, enhance mixing between and within sub-channels depending on their inclination in the flow domain. The attached vanes enhance the turbulent processes which lead to suppression of local Critical Heat Flux (CHF) [8] [9]. A commercial nuclear fuel assembly with a mixing vane can enhance CHF by up to 10% [8]. The geometry of the spacer grids also helps maintain gaps between fixed rods which serve the purpose of uniform distribution of hydro-dynamic properties of the flow. Despite the adverse increase of pressure drop in the rod bundle due to constriction of the coolant flow area by spacer grids, form drag and skin friction [10] resulting from the additional wall of the spacer grid, most nuclear fuel developments include the design of spacer grids with or without mixing vanes since their thermal hydraulic impact is too enormous to ignore. There are many efforts being made to develop an optimum spacer grid that can mix the flow effectively in sub-channel geometry [11]. Industrial designs of spacer grids are therefore assessed to satisfy desired optimum performance of sustained turbulence mixing whiles restraining pressure drops as much as possible. To achieve these enhancements, the mixing vane designs are optimized prior to their manufacture and application in the experimental investigation by the use of modern computational fluid dynamic codes. The application of computational fluid dynamic codes for design optimization makes it a less expensive practice than performing a number of experiments until the desired effects of the mixing device on the flow are realized.

The present work aims at investigating the extent of predictability of the mean and turbulent flow properties by the computational fluid dynamic code STAR-CCM+ for the flow of water through a 5 × 5 rod bundle supported by a spacer grid with and without a mixing vane. This was achieved by comparing simulation results

with experimental data obtained from the MATIS-H test facility at the Korea Atomic Energy Research Institute (KAERI). The study is relevant in assessing the suitability of the models employed to accurately predict the physical problem under study. Furthermore, the effect of the imposed interface topology on flow redistribution downstream of the spacer grid and hence on computational resource demand was also studied.

2. Methodology

2.1. Experimental

The MATIS-H (Measurement and Analysis of Turbulent Mixing in Sub-channels Horizontal) experiments performed at KAERI (Korean Atomic Energy Research Institute) to provide a set of data on the turbulent mixing due to split-type spacer grid in a rod bundle was employed in the present study. The experimental set up as described by Smith *et al.* [6] is illustrated in **Figure 4**.

Experimental data produced downstream of the spacer grid location included axial and lateral velocity components and root mean square velocity fluctuation which were used to measure the extent of predictability of the physical problem by the computational fluid dynamic code STAR-CCM+. Time-averaged data was reported along three line segments, Y1 = 16.56 mm, Y2 = 49.68 mm and Y3 = 82.8 mm as shown in **Figure 5** which is modified from the work of Podila *et al.* [1]. The data was collected at four axial positions of 0.5, 1.0, 4.0 and 10.0 of the hydraulic diameter from the tip of the mixing vane [12] [13].

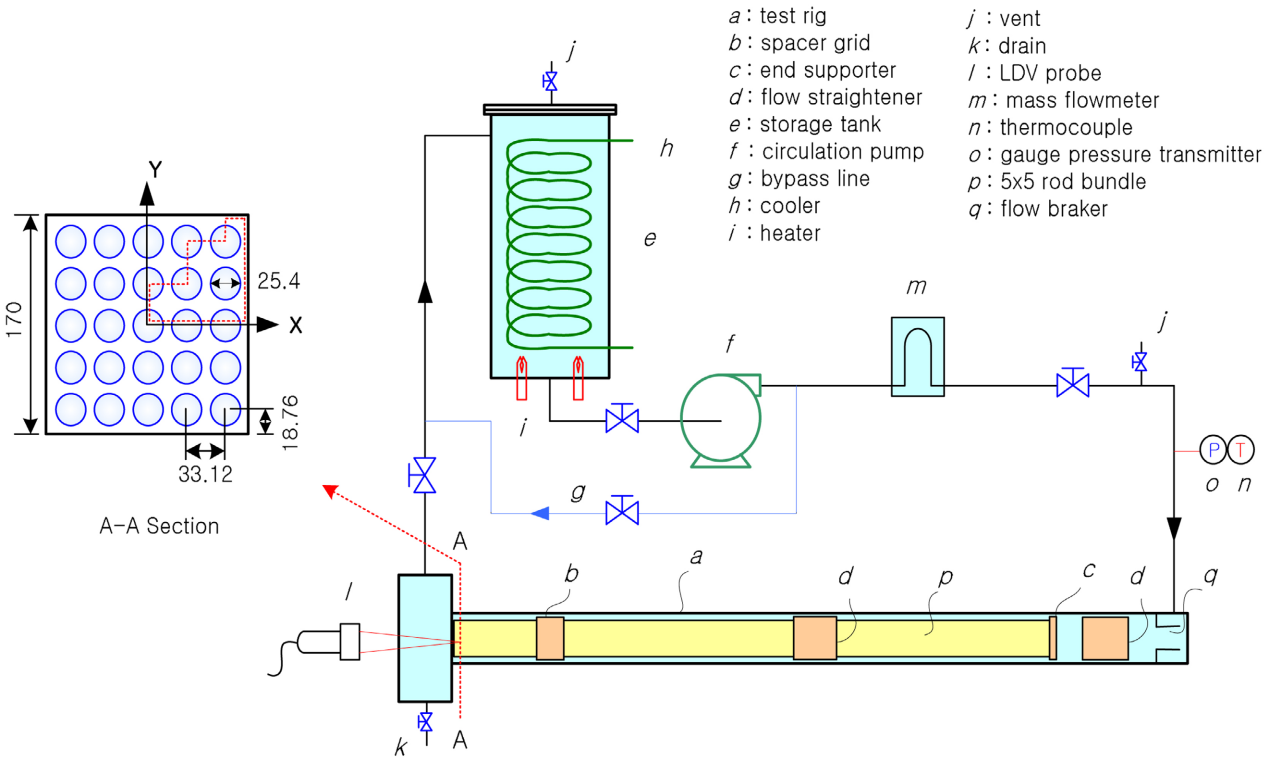

Figure 4. Schematic diagram of the MATIS-H test facility [6].

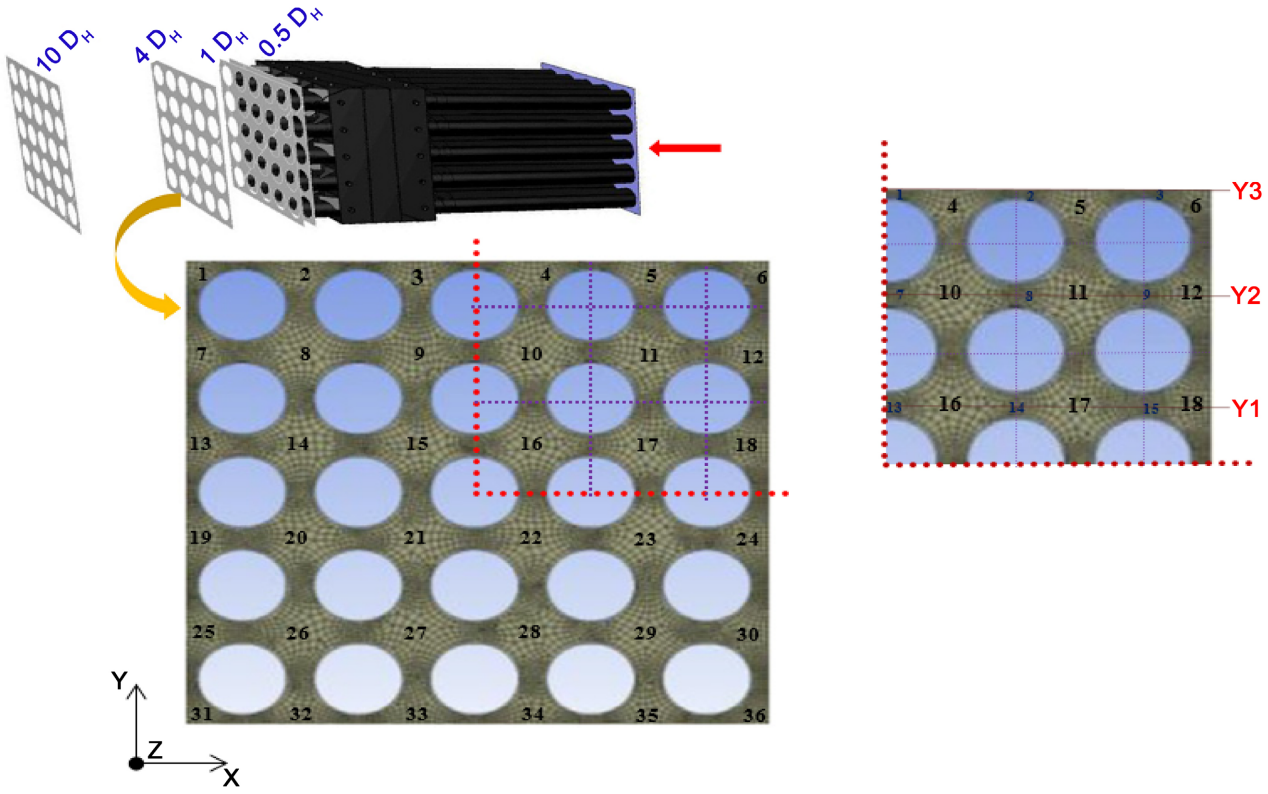

Figure 5. Positions for data extraction [12] [13].

2.2. STAR-CCM+ Simulation

Computer Aided Design (CAD) tools embedded in the Computational Fluid Dynamics code STAR-CCM+ were used in the present study to tailor and complete the domain which consisted of a square duct enclosing a 5 × 5 rod bundle arrangement which is supported in turn by a spacer grid with and without split mixing vanes. STAR-CCM+ was also used to generate mesh, set up physics models, solve and conduct post-processing of the results.

2.2.1. Geometry Modeling

The central, wall and corner sub-channels forming the entire domain of interest were modeled individually, duplicated and translated to their respective positions to form the geometry. Spacer grid CAD file made by using CATIA 5 obtained from KAERI was then imported a number of times and the Boolean operation "Subtract parts" applied at each import to subtracts the shape defined by the spacer grid with vanes from the volume of the sub-channel. Upon the Boolean operation, the surfaces of the imported spacer grid were imprinted in the target sub-channel. After identifying the inlet, outlet, and spacer grid boundaries the 3D CAD model was used to create a new geometry part with the named parts forming separate surfaces. The resulting fluid part was then assigned to region with the region mode set to one region per part and the boundary mode to one boundary per part surface. In-place interfaces were automatically formed and correctly defined. The new region has as its boundaries, the part surfaces defin-

ing the inlet, outlet, spacer grid and fluid volume. Velocity inlet, pressure outlet and no slip wall boundary types were assigned respectively and a geometry scene created to enable visualization of the final geometry which was used as sub-surface for mesh generation [12] [13].

2.2.2. Mesh Generation

Surface, polyhedral, prism and extruder meshing models were applied. The initial surface was re-tessellated so as to obtain a finer triangulation for generation of a high-quality volume mesh [5]. In the present study, the surface remesher was employed to re-triangulate and optimize the surface quality for volume meshing and also generate the sub-surface for the prism layer mesher. Table 1 shows the surface mesh parameters used in the present study [12] [13].

The polyhedral mesh type was selected considering such factors as, the turn-around time for building the mesh, the desired solution accuracy and convergence rate, the computational memory available, the quality of the starting surface mesh and quality of solution. The prism layer mesh model was used in conjunction with the core polyhedral mesh to generate orthogonal prismatic cells next to wall boundaries. The thickness of each cell layer was calculated using a geometric progression approach based on a constant size ratio. Table 2 shows the specification used for the prism layer in the present study.

Table 1. Surface mesh reference values.

Surface Mesh Reference Values	
Parameter	**Value**
Base Size	0.04 m
Automatic Surface Repairs	Activated
CAD Projection	Activated
Surface Curvature	Default
Surface Growth Rate	Default
Surface Proximity	Default
Absolute Minimum Size	0.002 m
Absolute Target Size	0.002 m

Table 2. Prism layer mesh reference values.

Prism Layer Mesh Reference Values	
Parameter	**Value (Fine Mesh)**
Number of Prism Layers	5
Prism Layer Stretching	1.3
Prism Layer Stretching Method	Geometric Progression
Prism Layer Thickness	
Absolute Size	0.002 m

The inlet and outlet boundaries of the completed geometry were extruded using the method of constant rate normal to extend the original domain along the z-axis to the required dimension in Figure 6. After a successful application of the meshing models, the meshed geometry generated is as illustrated in Figure 6. The mesh density and wall y^+ are 9.5 million and 11 respectively. Table 3 shows the extrusion mesh reference values [12] [13].

2.2.3. Setting up Physics Models

The physics continuum for single phase liquid (water) used for the present study consisted of the models shown in Table 4.

1) Material Modeling

Single component water which was the material simulated in the continuum was responsible for managing the various thermodynamic and transport properties and physical processes being modeled in the continuum. Table 5 illustrates the properties of water used in the present study [12] [13].

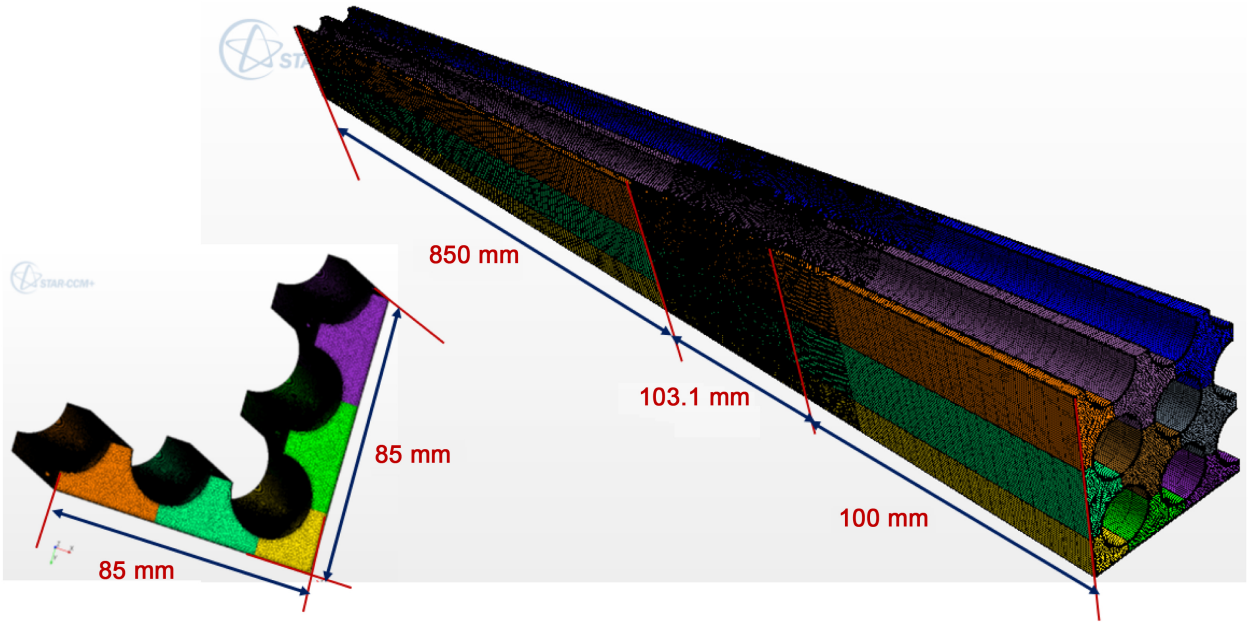

Figure 6. Mesh distribution and extent of quarter domain [12] [13].

Table 3. Extrusion mesh reference values.

Parameter	Inlet Boundary	Outlet Boundary
	Value (Fine Mesh)	Value (Fine Mesh)
Use Average Normal	activated	Activated
Magnitude	0.1	0.8
Number of Layers	25	140
Stretching	1.4	1.4
Create New Region	not activated	not activated

Table 4. Physics models.

Physics Models	
Model	**Mode Specification**
Space Model	3-Dimensional
Time Model	Steady State
Material Model	Liquid (Single Phase Water)
Equation of State Model	Constant Density
Flow Model	Segregated Flow
Energy Model	Segregated Fluid Isothermal
Viscous Regime Model	Turbulent
Turbulence Model	k-epsilum

Table 5. Water properties.

Continuum Properties	
Properties	**Values**
Temperature	35˚C
Density	994.06 kg/m^3
Dynamic Viscosity	7.1932×10^{-4} kg/ms
Specific Heat	4179.1 J/kgK
Thermal Conductivity	0.62335 W/mK
Turbulent Prandtl Number	0.9

2) Turbulence Modeling

The three turbulence models employed for this work are the realizable two-layer k-epsilon model, the non-linear standard k-epsilon model and the SST-k-Omega model [5]. Although it is strictly possible to simulate turbulent flow directly by resolving all the scales of the flow (termed direct numerical simulation), the computer resources required are too large for practical flow simulations [5]. Therefore, a suitable turbulence modeling approach which provides closure of the governing equations in turbulent flows must be employed. Most simulations rely on models that provide closure for the Reynolds Average Navier Stokes (RANS) equations. The challenge in turbulence modeling however is the model of the Reynolds stress tensor in terms of the mean flow quantities. The eddy viscosity model and the Reynolds stress transport models are the two basic approaches employed for modeling the stress tensor which is expressed as [5].

$$\boldsymbol{T}_t = \rho\overline{u'u'} = \rho\begin{bmatrix} \overline{u'u'} & \overline{u'v'} & \overline{u'w'} \\ \overline{u'v'} & \overline{v'v'} & \overline{v'w'} \\ \overline{u'w'} & \overline{v'w'} & \overline{w'w'} \end{bmatrix} \tag{1}$$

For the present study, k-epsilon turbulence model which is a two-equation

model that solves transport equations of turbulent kinetic energy k and its dissipation rate ε was employed. The inherent approach employed to model the stress tensor is therefore the eddy viscosity model which is based on the concept of turbulence viscosity. The most common eddy viscosity model is the Boussinesq approximation which is given by Equation (2) [5].

$$\rho\overline{u'u'} = 2\mu_t \boldsymbol{S} - \frac{2}{3}\left(\mu\nabla\cdot\boldsymbol{v} + \rho k\right)\boldsymbol{I} \tag{2}$$

where, k is the turbulent kinetic energy and $\boldsymbol{S}$ is the strain tensor computed from the resolved velocity fields $\boldsymbol{v}$. Although the k-epsilon model also exists in its standard form, the realizable two-layer model was adopted for the present investigation. The realizable two-layer k-epsilon model combines the realizable k-epsilon model with the two-layer model and hence gains added flexibility of an all-y^+ wall treatment. An all-y^+ wall treatment is a hybrid approach designed to give results similar to the low-y^+ wall treatment as $y^+ \to 0$ and to the high-y^+ wall treatment for $y^+ > 30$. It will also give reasonable results for intermediate meshes where the cell centroid falls in the buffer layer [5]. The dimensionless wall distance y^+ is related to the wall distance y from the first prism layer cell by,

$$y^+ = \frac{y}{v}\sqrt{\frac{\tau_w}{\rho}} \tag{3}$$

where, τ_w is wall shear stress, ρ is density and v is kinematic viscosity.

The realizable k-epsilon model developed by Shih *et al.* [14] contains a new transport equation for the turbulent dissipation rate ε and also, a critical coefficient of the model C_μ, expressed as a function of mean flow and turbulence properties, rather than assumed to be constant as in the standard k-epsilon model. This allows the model to satisfy certain mathematical constraints on the normal stresses consistent with the physics of turbulence. For the realizable k-epsilon model [5], the turbulent viscosity in the transport equation is evaluated by Equation (4).

$$\mu_t = \rho C_\mu \frac{k^2}{\varepsilon} \tag{4}$$

where, the coefficient C_μ is no longer constant as with the standard k-epsilon model, but is instead given by Equation (5) [5],

$$C_\mu = \frac{1}{A_o + A_s U^{(*)}\frac{k}{\varepsilon}} \tag{5}$$

The coefficients defining the model have the following values [5],

$$C_{\varepsilon 2} = 1.9,\quad \sigma_k = 1.0,\quad \sigma_\varepsilon = 1.2$$

$$C_{\varepsilon 1} = \max\left(0.43, \frac{\eta}{5+\eta}\right) \tag{6}$$

$$\eta = \frac{Sk}{\varepsilon} \tag{7}$$

where, the turbulent kinetic energy (k) is derived from a specified turbulent intensity (I) and local velocity (v) by the relation,

$$k = \frac{3}{2}(Iv)^2 \tag{8}$$

and the modulus of the mean strain rate tensor S and the strain tensor $\boldsymbol{S}$ are expressed as,

$$S = |\boldsymbol{S}| = \sqrt{2\boldsymbol{S}:\boldsymbol{S}} \tag{9}$$

$$\boldsymbol{S} = \frac{1}{2}\left(\nabla \boldsymbol{v} + \nabla \boldsymbol{v}^{\mathrm{T}}\right) \tag{10}$$

The two-layer approach, first suggested by Rodi [15], is an alternative to the low-Reynolds number approach that allows the k-epsilon model to be applied in the viscous sub-layer. In this approach, the computation is divided into two layers. In the layer adjacent to the wall, the turbulent dissipation rate ε and the turbulent viscosity μ_t are specified as functions of wall distance. The values of ε specified in the near-wall layer are blended smoothly with the values computed from solving the transport equation far from the wall. The equation for the turbulent kinetic energy is solved in the entire flow. The realizable models implemented with a two-layer approach, enables resolution of the viscous sub-layer when used with fine meshes. The two-layer model is parameterized as a length scale function, $l_\varepsilon = f\left(y, \mathrm{Re}_y\right)$ and a turbulent viscosity ratio function, $\mu_t/\mu = f\left(\mathrm{Re}_y\right)$. The dissipation rate computed from the two-layer model is evaluated as [5],

$$\varepsilon = \frac{k^{3/2}}{l_\varepsilon} \tag{11}$$

The two-layer model blends a one-equation model. According to the Wolfstein one equation model [5],

$$l_\varepsilon = C_1 y\left[1 - \exp\left(\frac{\mathrm{Re}_y}{A_\varepsilon}\right)\right] \tag{12}$$

where, $A_\varepsilon = 2C_1$ and $C_1 = \kappa C_\mu^{3/2}$.

$$C_\mu = 0.09 \quad \text{and} \quad \kappa = 0.42$$

The turbulent viscosity is computed from Equation (13) [5],

$$\frac{\mu_t}{\mu} = \mathrm{Re}_y C_\mu^{1/4}\kappa\left[1 - \exp\left(\frac{\mathrm{Re}_y}{A_\mu}\right)\right] \tag{13}$$

where, $\mathrm{Re}_y = \sqrt{ky}/v$ and $A_\mu = 70$.

The model coefficients for the cubic constitutive correlation as described in Baglietto *et al.* [16] were applied for the non-linear standard k-epsilon (NLS-K-E) model.

The under relaxation factors for the turbulence solver that controls the solution of the k-epsilon models (k and ε) and the turbulent viscosity solver that controls the update of turbulent viscosity were under-relaxed for the flow solu-

tion to be stable and hence converged. The algebraic multigrid parameters were kept at default conditions for the present simulation [12] [13].

3. Results and Discussion

Data was compared over line probe located at the lateral position Y1 and axial position of 1.0 hydraulic diameter from the tip of the mixing vane as shown in Figure 5. Figure 7 shows the location of the line probe for data analysis as presented in this section.

3.1. Validation and Verification of Simulation Results

The extent of predictability of the spacer effect by CFD was determined by comparing trends of the experimental data with the simulation results. Figures 8-11 show the comparison of mean and turbulent flow parameters of the simulation to the experimental for the case of spacer grid with split vane at the spanwise (x-component velocity), transverse (y-component velocity) and axial (z-component velocity) directions respectively. In the legend of Figures 8-11, "SPV" refers to case of spacer grid with split vane, "EXP" refers to trends of experimental data "SIM" refers to trends of simulation data and "RE1" is the

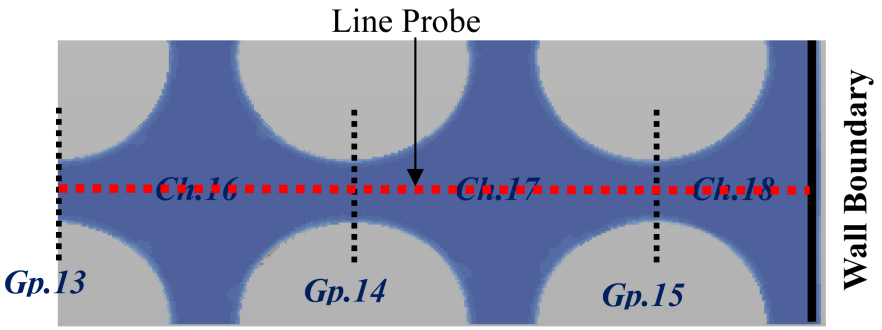

Figure 7. Position of line probe.

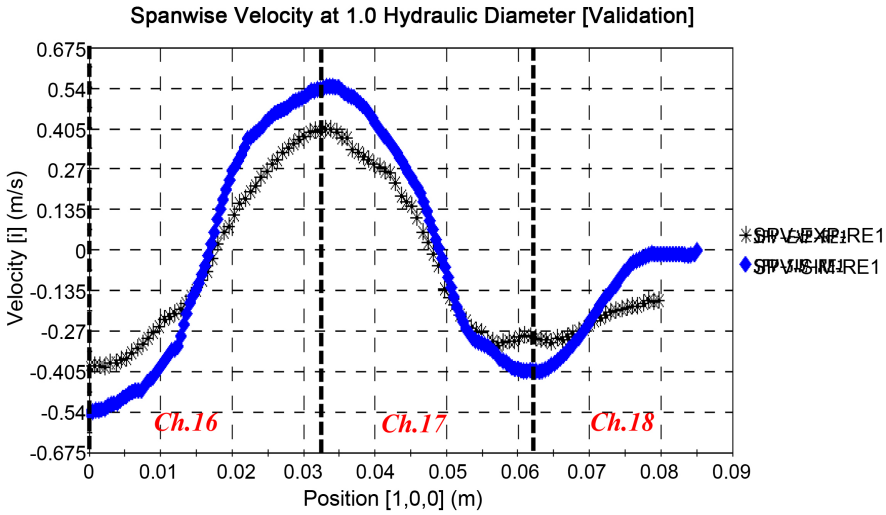

Figure 8. Validation of spanwise velocity data.

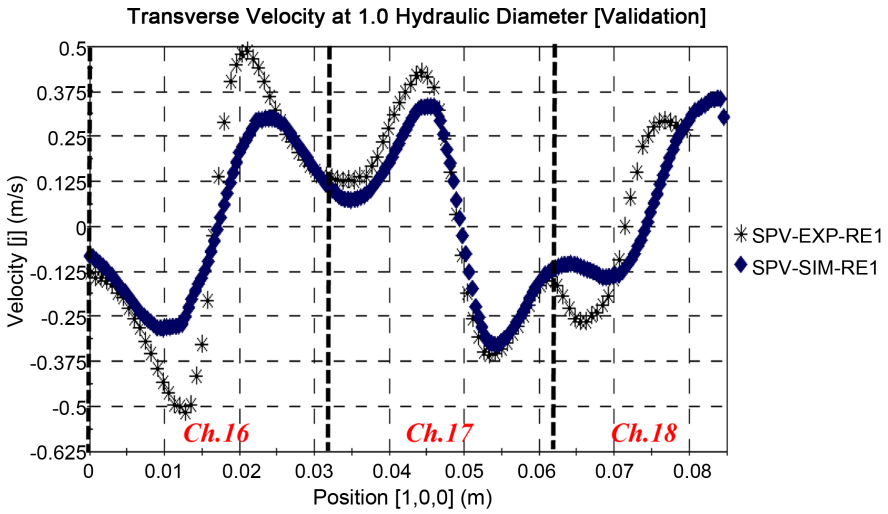

Figure 9. Validation of transverse velocity data.

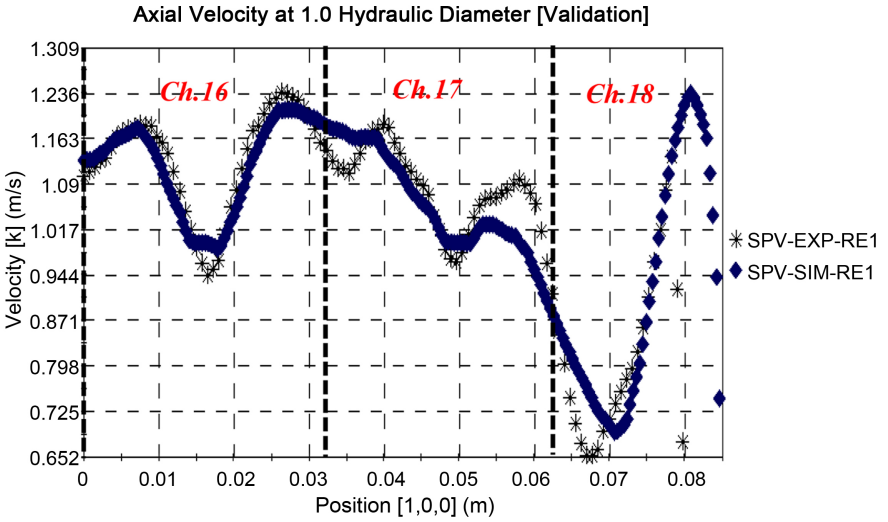

Figure 10. Validation of axial velocity data.

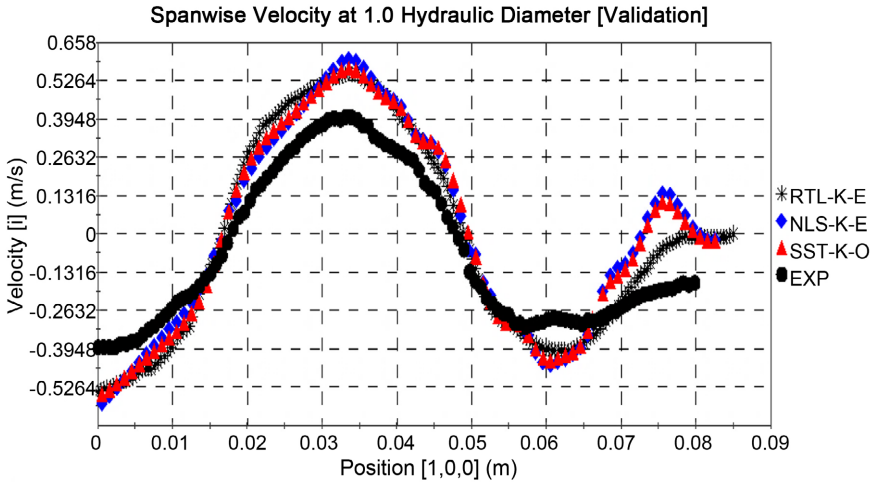

Figure 11. Verification of spanwise velocity data.

Reynolds number at which the simulation was performed and has a magnitude of 3.4×10^4.

In Figure 8, the spanwise velocity distribution from the simulation is compared with that of the experimental data.

As observed in Figure 8, good agreement of the simulation results for the spanwise velocity is obtained. Similar agreement was also realized in the investigation performed by Podila *et al*. [1], Frank *et al*. [17], Batta and Class [18] and Lee *et al*. [19]. Figure 8 showed departure of the simulation results from the experimental especially at the maxima and minima locations. Higher extents of cross-flow are predicted in the gap regions for the simulation results than for the experimental data. The short dash black lines show the gap locations for a pitch of 33.12 mm. Appreciable agreement of the simulation data with the experimental data are made for velocity in the transverse direction at the gap locations as shown in Figure 9 although some level of deviations of the simulation data from the experimental are observed at the maxima and minima.

The axial velocity distribution as depicted in Figure 10 also showed appreciable agreement of simulation data with the experimental observations generally and especially in the gaps. Similar agreements were also reported by Kang *et al*. [20] and Chang *et al*. [11].

Results obtained by the application of the realizable k-epsilon model with linear constitutive relation (RTL-K-E) was verified with other turbulence models such as the non-linear standard k-epsilon model (NLS-K-E) as applied in Baglietto *et al*. [16] with a cubic constitutive relation, and the SST-k-Omega model (SST-K-O). The results are shown in Figures 11-13.

The mesh parameters for the turbulent models in Figures 11-13 are compared in Table 6.

As observed in Figures 11-13, appreciable agreement of the simulation results of the RTL-K-E model with the NLS-K-E model and the SST-K-O models is evident for the mean flow parameters. Holloway *et al*. [21] in their investigation attributed the success of the SST-K-O model to their near wall treatment

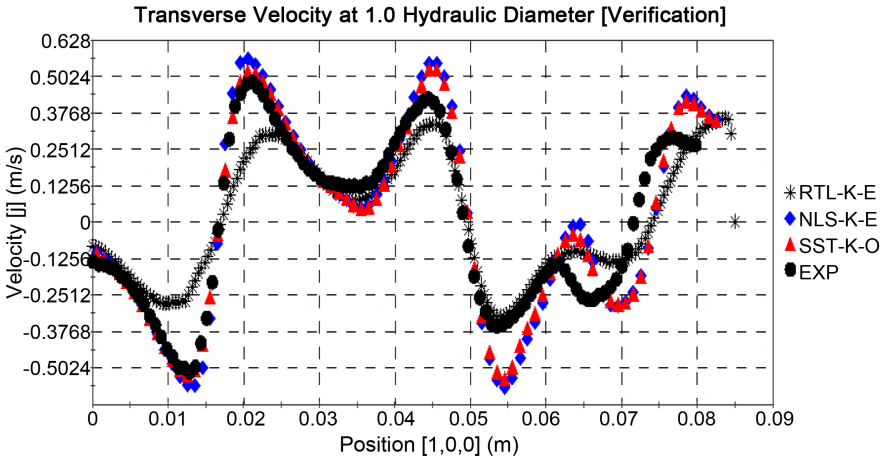

Figure 12. Verification of transverse velocity data.

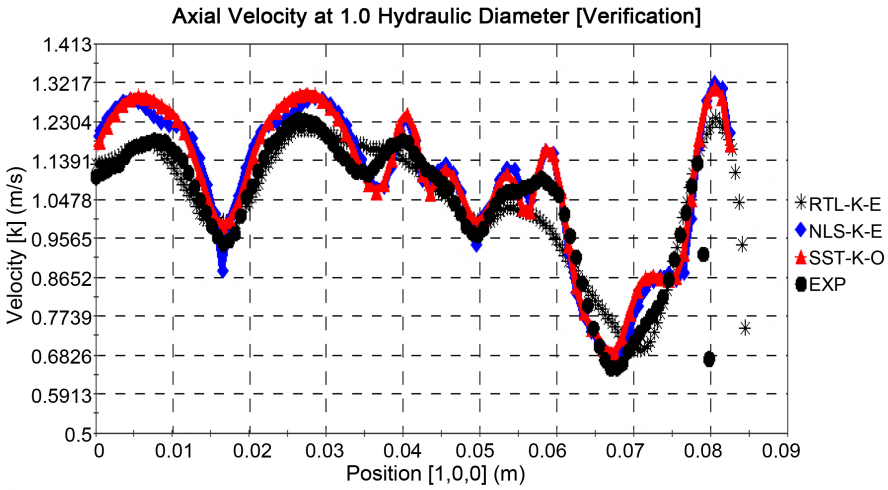

Figure 13. Verification of axial velocity data.

Table 6. Comparison of mesh parameters.

Case of Split Vane at Re1			
	RTL-K-E	**NLS-K-E**	**SST-K-O**
y^+	11	31	31
Mesh Density	9.5 M	6.4 M	6.4 M
Core Mesh Type	Polyhedral	Trimmer	Trimmer
Wall Treatment	All y^+	High y^+	High y^+
Number of Prism Layers	5	4	4
Prism Layer Thickness	0.002 m	0.001 m	0.001 m
Extent of Domain	Full, z = 1.1 m	Half, z = 0.7 m	Half, z = 0.7 m

which relies on damping of the turbulent viscosity in low Reynolds number regions rather than a two-layer wall treatment as implemented in the RTL-K-E model. A better prediction by the SST-K-O model and the non-linear models are also attested to in the works of Holloway *et al*. [21], Ruifeng *et al*. [22], Gandhir *et al*. [23] and Horvath *et al*. [24]. Consistent with the findings of Yang *et al*. [25], Zhu *et al*. [26] established in their analysis appreciable prediction by the standard two-layer k-epsilon model than the realizable two-layer k-epsilon model.

3.2. Effect of Interface Topology on Flow Distribution

3.2.1. Case of Spacer Grid without Mixing Vanes

Figure 14 and **Figure 15** show a comparison of curves of axial velocity at a lateral position of Y1 as shown in **Figure 5** for the case of flow of water through a square duct that encloses a 5 × 5 rod bundle arrangement and a spacer grid without mixing vanes. For each graph, simulation data were compared for the

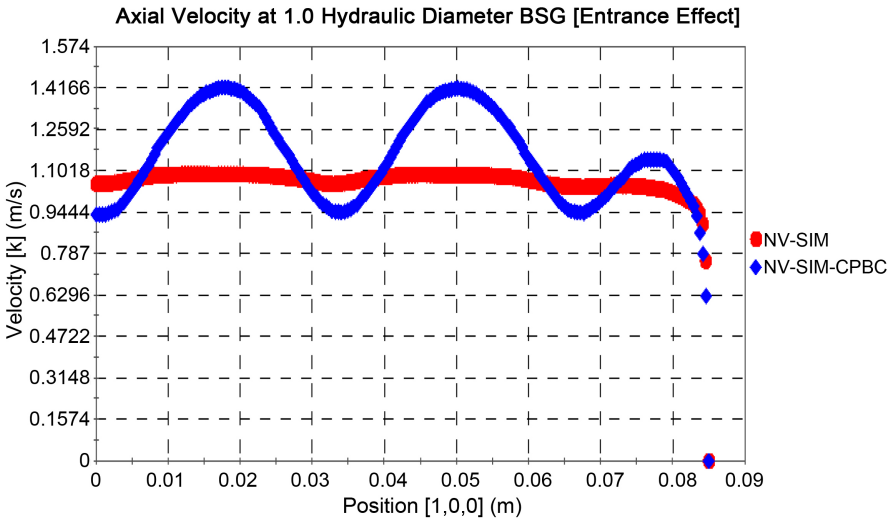

Figure 14. Effect of interface topology on axial velocity distribution before spacer grid location [No-Vane].

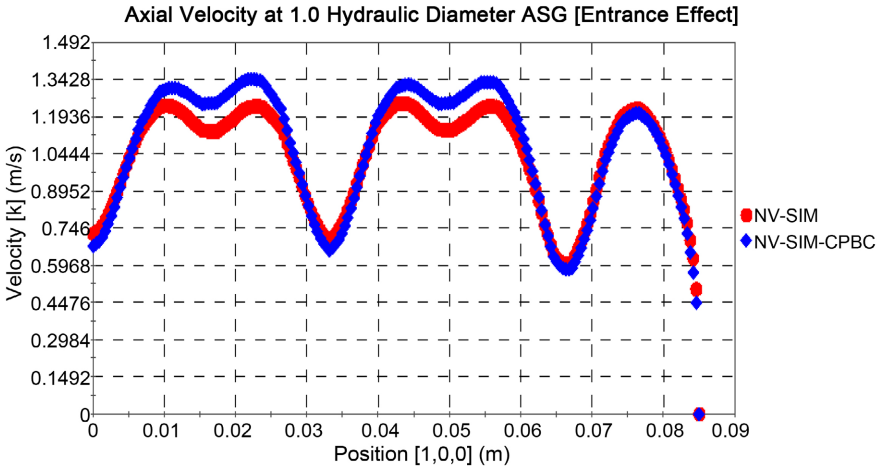

Figure 15. Effect of interface topology on axial velocity distribution after spacer grid location [No-Vane].

case that involved the imposition of periodic boundary condition (NV-SIM-CPBC) and the other with no imposed periodic boundary condition (NV-SIM) at the inlet-outlet boundaries at axial positions of 0.5 hydraulic diameters Before Spacer Grid (BSG) and 1.0 hydraulic diameter After Spacer Grid (ASG).

Large variations in the trend of axial velocity are noticed between the two interface topology types Before Spacer Grid (BSG) as observed in **Figure 14**. The deviation has however narrowed after flow through the spacer grid as seen in **Figure 15**. The upstream effect on flow due to differences in interface topology are however still prominent downstream of the spacer grid without mixing vane, as observed in **Figure 15**. Thus, much longer segment of the domain is required in order to nullify the entrance effect on the downstream of flow parameters.

The comparison of the interface topology effect on turbulent intensity in the presence and absence of mixing vanes is as shown in **Figure 16** and **Figure 17**.

As in Figure 16, large deviations in turbulent intensity profile of the two different topology types is observed at entry of flow to the spacer grid which is depicted by Figure 16. At exit of the spacer grid, although the variation in trend reduced drastically, an appreciable difference is profile especially at the maxima is noticeable in Figure 17. This observation indicates that in the absence of mixing vanes, the effect of the imposed inlet-outlet interface topology type on mean and turbulent flow parameters cannot be neglected immediately downstream of the spacer grid.

3.2.2. Case of Spacer Grid with Split Mixing Vanes

As observed for the case of spacer grid without attached mixing vanes, the inlet-outlet interface topology effect was evident even after flow through the spacer grid. In the presence of mixing vanes however, the deviations observed in the curves upstream were almost completely cancelled downstream of the spacer grid as shown in Figure 18 and Figure 19. Thus shorter segment of the domain than required for the case of flow through a spacer grid without vane is needed

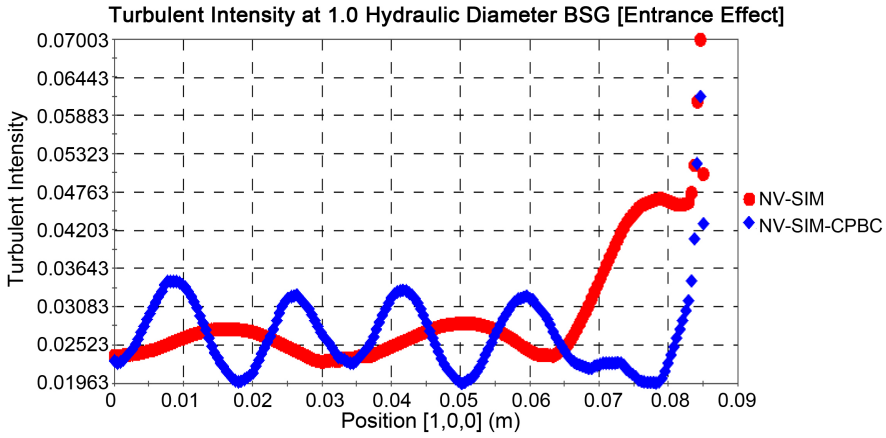

Figure 16. Effect of interface topology on turbulent intensity distribution before spacer grid location [No-Vane].

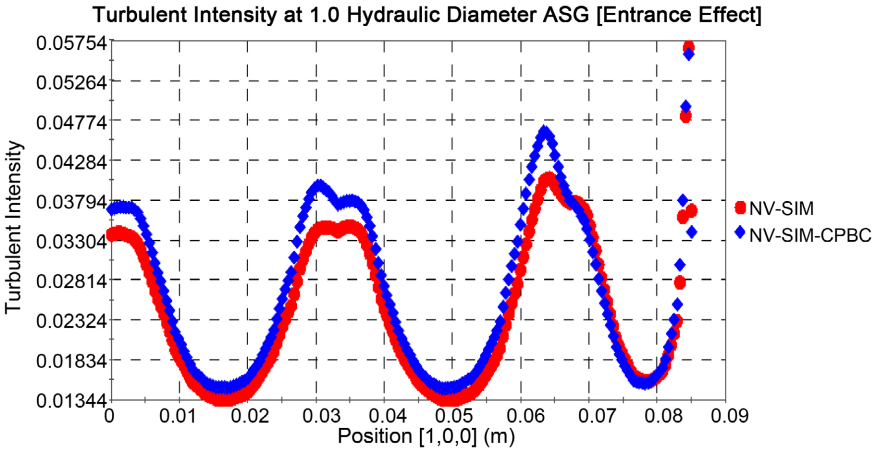

Figure 17. Effect of interface topology on turbulent intensity distribution after spacer grid location [No-Vane].

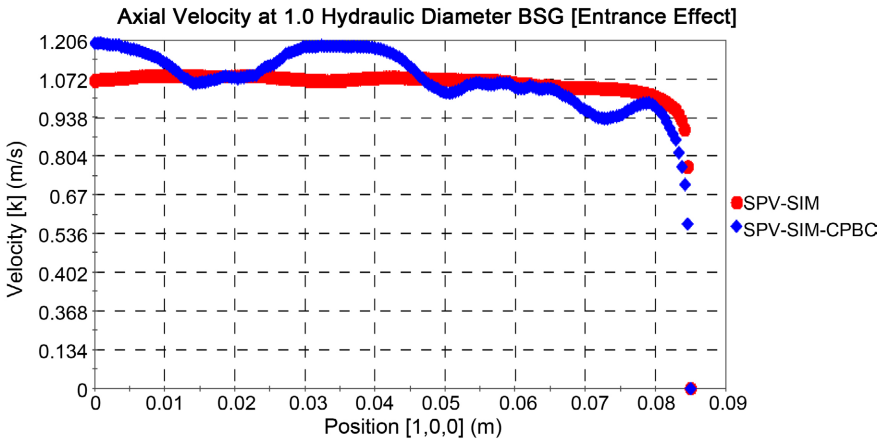

Figure 18. Effect of interface topology on axial velocity distribution before spacer grid location [Split-Vane].

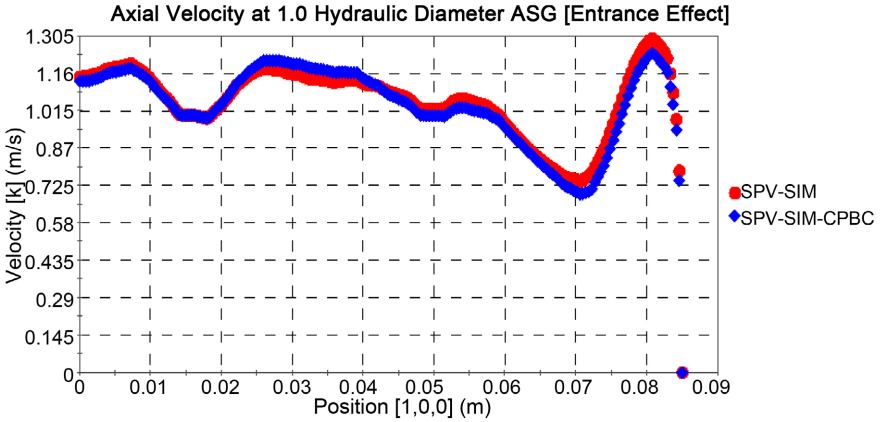

Figure 19. Effect of interface topology on axial velocity distribution after spacer grid location [Split-Vane].

to conceal the effect of the inlet-outlet interface topology on flow development downstream of a spacer grid with attached split mixing vanes. The computational resource demand when modeling flow through a spacer grid with split mixing vanes would therefore be appreciably lower than in the absence of mixing vanes.

Comparison of **Figure 20** and **Figure 21** also show a complete nullification of the interface topology effect on the turbulent parameter in the presence of mixing vanes at exit of the spacer grid.

The independence of the mean and turbulent flow parameter distribution at 1.0 hydraulic diameter downstream of the spacer grid on interface topology for the case of flow of water through a spacer grid with split mixing vanes is attributed to the additional pressure drop at this location due to the mixing vanes. **Table 7** shows line averaged pressure drop values across the spacer grid obtained over line probes positioned at spacer inlet and at 1.0 hydraulic diameter from the exit face of the spacer grid. The split vane effects (ratio of pressured drop in the presence of split vane to pressure drop in the absence of split vane) at lateral

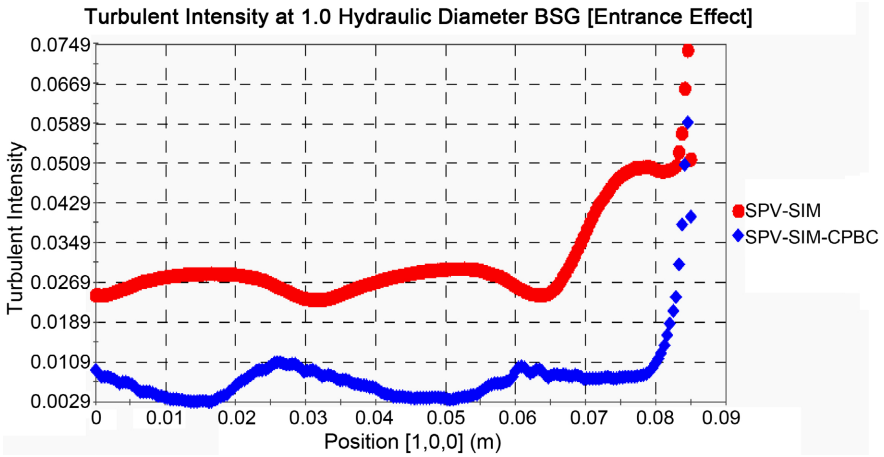

Figure 20. Effect of interface topology on turbulent intensity distribution before spacer grid location [Split-Vane].

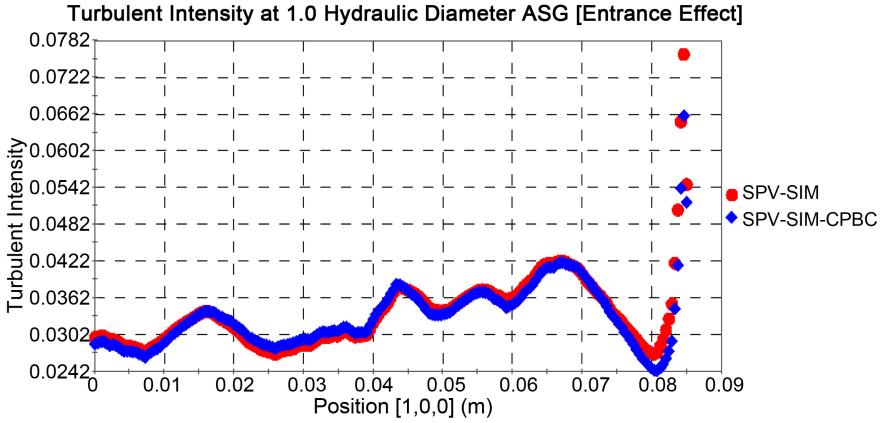

Figure 21. Effect of interface topology on turbulent intensity distribution after spacer grid location [Split-Vane].

Table 7. Vane effect on pressure drop across spacer grid.

Average Pressure Drop (Pa) at 1.0 Hydraulic Diameter				
		Y1	**Y2**	**Y3**
$Re1 = 3.4 \times 10^4$	*SPLIT-VANE*	865	837	777
	NO-VANE	617	611	603
	Vane Effect	**1.40**	**1.37**	**1.29**
$Re2 = 8.5 \times 10^4$	*SPLIT-VANE*	4991	4826	4423
	NO-VANE	3464	3417	3370
	Vane Effect	**1.44**	**1.41**	**1.31**
$Re3 = 1.7 \times 10^5$	*SPLIT-VANE*	18,101	17,532	15,867
	NO-VANE	12,266	12,166	12,046
	Vane Effect	**1.48**	**1.44**	**1.32**
$Re4 = 2.6 \times 10^5$	*SPLIT-VANE*	39,132	37,962	34,317
	NO-VANE	26,160	26,002	25,707
	Vane Effect	**1.50**	**1.50**	**1.33**

positions Y1, Y2 and Y3 as in Figure 5 for the four Reynolds numbers employed in the present study are also tabulated.

At the lateral position Y1, Table 7 shows an increase in pressure drop due to the mixing vane by 40% at Re1, 44% at Re2, 48% at Re3 and 50% at Re4. These large increases in pressure drops that are also observed at lateral positions Y2 and Y3 led to a reduction in momentum and subsequent deceleration in the flow such that much time was available to attain a more developed redistribution just behind the mixing vanes than for the case of spacer grid without vanes for which no deceleration in the axial flow due to mixing vanes is present.

4. Conclusions

1) In the present study, the suitability of STAR-CCM+ to predict mean and turbulent flow parameters for a new design of spacer grid with split mixing vanes which supported a 5 × 5 rod bundle arrangement and enclosed in a square duct was assessed.

2) Polyhedral meshing model was employed to discretize the flow domain and the segregated flow model which solves the flow equations, one for each component of velocity herein termed as spanwise (x-component), transverse (y-component) and axial (z-component) and one for pressure in an uncoupled manner was used to model the single phase, steady state, incompressible flow in the present study. The segregated fluid isothermal model was applied as the energy model to provide a constant temperature field of 35 degrees for all models that required temperature. The realizable two-layer k-epsilon turbulent model was adopted to model the transported variables of production and dissipation of turbulent kinetic energy.

3) Comparison of simulation results with experimental data showed a good prediction of the mean flow parameters by the models employed in STAR-CCM+ which indicates the suitability of the commercial software for the analysis of the physical problem.

4) Comparison of mean flow parameters before and after the passage of flow through spacer grids with and without mixing vanes showed the effect of the mixing vanes to quickly bring the flow to an equal redistribution downstream of the spacer grid irrespective of the inlet-outlet interface topology. For the case of the spacer grid without mixing vanes, the inlet-outlet interface topology influenced the distribution of the flow downstream of the spacer grid. The observation indicates that a much longer inlet segment of the domain is required to completely nullify the effect of the inlet-outlet interface topology on flow distribution in the absence of mixing vanes than in the presence of mixing vanes which may lead to a relatively higher demand for computational resource. The observation was associated with the additional pressure drop caused by the presence of mixing vanes and the retardation of flow by the mixing vanes resulting from flow interaction of the axial flow by lateral convection.

Acknowledgements

CD-Adapco is acknowledged for providing technical support for this work.

Conflicts of Interest

The authors declare no conflicts of interest regarding the publication of this paper.

References

[1] Podila, K., Rao, Y.F., Krause, M. and Bailey, J. (2014) A CFD Simulation of 5x5 Rod Bundle with Split-Type Spacers. *Progress in Nuclear Energy*, **70**, 167-175. https://doi.org/10.1016/j.pnucene.2013.08.012

[2] Krauss, T. and Meyer, L. (1996) Characteristics of Turbulent Velocity and Temperature in a Wall Channel of a Heated Rod Bundle. *Experimental Thermal Fluid Science*, **12**, 75-86. https://doi.org/10.1016/0894-1777(95)00076-3

[3] Baglietto, E. and Ninokata, H. (2005). A Turbulence Model Study for Simulating Flow inside Tight Lattice Rod Bundle. *Nuclear Engineering and Design*, **235**, 773-784. https://doi.org/10.1016/j.nucengdes.2004.10.007

[4] Caraghiaur, D., Anglart, H. and Frid, W. (2009) Experimental Investigation of Turbulent Flow through Spacer Grid in Fuel Rod Bundles. *Nuclear Engineering and Design*, **239**, 2013-2021. https://doi.org/10.1016/j.nucengdes.2009.05.029

[5] CD-Adapco User Guide, STAR-CCM+, Version 6.04.014 (2011).

[6] Smith, B.L., Song, C.H., Chang, S.K., Lee, J.R. and Kim, J.W. (2013) Report of the OECD/NEA-KAERI Rod Bundle CFD Benchmark Exercise. NEA/CSNI/R 5, 4-124.

[7] Jayanti, S. and Rajesh Reddy, K. (2013) Effect of Spacer Grids on CHF in Nuclear Rod Bundle. *Nuclear Engineering and Design*, **261**, 66-75. https://doi.org/10.1016/j.nucengdes.2013.03.044

[8] De Crecy, F. (1994) The Effect of Grid Assembly Mixing Vanes on CHF Values and Azimuthal Locations in Fuel Assemblies. *Nuclear Engineering and Design*, **149**, 233-241. https://doi.org/10.1016/0029-5493(94)90289-5

[9] Shin, B.S. and Chang, S.H. (2003) An Experimental Work on the Relation between Flow Structure and CHF by Various Spacer Grids in 2x2 Rod Bundle with R-134a. *The* 10*th International Topical Meeting on Nuclear Reactor Thermal Hydraulics* (*NURETH*-10), Seoul, 5-11 October 2003, 5-9.

[10] Avramova, M. (2007) Development of an Innovative Spacer Grid Model Utilizing Computational Fluid Dynamics within a Sub-channel Analysis Tool. Doctoral Dissertation, The Pennsylvania State University, State College, 75-146.

[11] Chang, S.K., Moon, S.K., Bok Deuk Kim, B.D., Baek, W.P. and Choi, Y.D. (2008) Phenomenological Investigation on the Turbulent Flow Structures in a Rod Bundle Array with Mixing Devices. *Nuclear Engineering and Design*, **238**, 600-609. https://doi.org/10.1016/j.nucengdes.2007.02.037

[12] Agbodemegbe, V.Y., Cheng, X., Akaho, E.H.K. and Allotey, F.K.A. (2016) An Investigation of the Effect of Split-Type Mixing Vane on Extent of Crossflow between Subchannels through the Fuel Rod Gaps. *Annals of Nuclear Energy*, **88**, 174-185. https://doi.org/10.1016/j.anucene.2015.10.036

[13] Agbodemegbe, V.Y., Cheng, X., Akaho, E.H.K. and Allotey, F.K.A. (2015) Correlation for Cross-Flow Resistance Coefficient Using STAR-CCM+ Simulation Data for Flow of Water through Rod Bundle Supported by Spacer Grid with Split-Type Mixing Vane. *Nuclear Engineering and Design*, **285**, 134-149. https://doi.org/10.1016/j.nucengdes.2015.01.003

[14] Shih, T., Liou, W.W., Shabbir, A., Yang, Z. and Zhu, J. (1994) A New K-Eddy Vis-

cosity Model for High Reynolds Number Turbulent Flows Model Development and Validation. NASA TM 106721.

[15] Rodi, W. (1991) Experience with Two-Layer Models Combining the k-ε Model with a One-Equation Model near the Wall. 29*th Aerospace Sciences Meeting*, Reno, 7-10 January 1991, AIAA 91-0216. https://doi.org/10.2514/6.1991-216

[16] Baglietto, E., Ninokata, H. and Misawa, T. (2006) CFD and DNS Methodologies for Fuel Bundle Simulations. *Nuclear Engineering and Design*, **233**, 1503-1510. https://doi.org/10.1016/j.nucengdes.2006.03.045

[17] Frank, Th., Jain, S., Matyushenko, A.A. and Garbaruk, A.V. (2012) The OECD/NEA MATIS-H Benchmark-CFD Analysis of Water Flow Through a 5 × 5 Rod Bundle with Spacer Grids Using ANSYS FLUENT and ANSYS CFX. *Conference on Experimental Validation and Application of CFD and CMFD Codes in Nuclear Reactor Technology*, *OECD/NEA and IAEA Workshop*, Daejeon, 10-12 September 2012, 1-37.

[18] Batta, A. and Class, A.G. (2013) CFD (Computational Fluid Dynamics) Study of Isothermal Water Flow in Rod Bundles with Split-Type Spacer Grids: OECD/NEA Benchmark MATIS-H. *Conference*: *SNA & MC* 2013, Paris, 27-31 October 2013, 1-6.

[19] Lee, J.R., Kim, J. and Song, C.H. (2014) Synthesis of the Turbulent Mixing in a Rod Bundle with Vaned Spacer Grids Based on the OECD-KAERI CFD Benchmark Exercise. *Nuclear Engineering and Design*, **279**, 3-18. https://doi.org/10.1016/j.nucengdes.2014.03.008

[20] Kang, H.S., Chang, S.K. and Song, C.-H. (2012) CFD Analysis of the MATIS-H Experiments on the Turbulent Flow Structures in a 5 × 5 Rod Bundle with Mixing Devices. CFD4NRS-3: Computational Fluid Dynamics (CFD) for Nuclear Reactor Safety Applications—Experimental Validation and Application of CFD and CMFD Codes to Nuclear Reactor Safety Issues (1), NEA-CSNI-R—2011-14, 1-10.

[21] Holloway, M.V., Beasley, D.E. and Corner, M.E. (2006) Investigation of Swirling Flow in Rod Bundle Subchannels Using Computational Fluid Dynamics. *Proceedings of ICON*14, *International Conference on Nuclear Technology*, Miami, 17-20 July 2006, 1-11.

[22] Tian, R., *et al.* (2012) Single-Phase Computational Fluid Dynamics Applicability for the Study of Three-Dimensional Flow in 5 × 5 Rod Bundles with Spacer Grids. *Chinese Journal of Mechanical Engineering*, **25**, 738-744.

[23] Gandhir, A. and Hassan, Y. (2011) RANS Modeling for Flow in Nuclear Fuel Bundle in Pressurized Water Reactors (PWR). *Nuclear Engineering and Design*, **241**, 4404-4408. https://doi.org/10.1016/j.nucengdes.2011.08.084

[24] Horvath, A. and Dressel, B. (2012) Numerical Simulations of Square Arrayed Rod Bundles. *Nuclear Engineering and Design*, **247**, 168-182. https://doi.org/10.1016/j.nucengdes.2012.03.004

[25] Yang, J., Oka, Y., Ishiwatari, Y., Liu, J. and Yoo, J. (2007) Numerical Investigation of Heat Transfer in Upward-flows of Supercritical Water in Circular Tubes and Tight Fuel Rod Bundles. *Nuclear Engineering and Design*, **237**, 420-430. https://doi.org/10.1016/j.nucengdes.2006.08.003

[26] Zhu, X., Morooka, S. and Oka, Y. (2014) Numerical Investigation of Grid Spacer Effect on Heat Transfer of Supercritical Water Flows in a Tight Rod Bundle. *International Journal of Thermal Sciences*, **76**, 245-257. https://doi.org/10.1016/j.ijthermalsci.2013.10.003

Abbreviations — Definition

OECD	Organization for Economic Co-operation and Development
NEA	Nuclear Energy Agency
MATIS-H	Measurement and Analysis of Turbulent Mixing In Sub-Channels-Horizontal
EXP	Experimental
Re	Reynolds Number
SPV	Split Vane
NV	No Vane
SST-K-O	Shear Stress Transport K-Omega
NLS-K-E	Non-Linear Standard K-Epsilon
RTL-K-E	Realizable Two-Layer K-Epsilon
BSG	Before Spacer Grid
ASG	After Spacer Grid
CPBC	Cyclic Periodic Boundary Condition

Nomenclature

C_μ	Model Coefficient
I	Identity Matrix
k	Turbulent Kinetic Energy
l_ε	Length Scale
Re_y	Wall Distance-based Reynolds Number
$\boldsymbol{S}$	Modulus of the Mean Strain Rate Tensor
S	Strain Tensor
$\boldsymbol{T}_t$	Turbulent Stress Tensor
u'	Lateral Fluctuating Velocity in X-Direction
v'	Lateral Fluctuating Velocity in the Y-Direction
w'	Axial Fluctuating Velocity in the Z-Direction
y	Wall Distance
y^+	Wall Dimensionless Distance

Greek Letters

ε	Turbulent Dissipation Rate
μ_t	Turbulent Viscosity
ρ	Density
τ_w	Wall Shear Stress